nature portfolio

https://doi.org/10.1038/s41586-025-10042-w

Supplementary information

Laser writing in glass for dense, fast and efficient archival data storage

In the format provided by the authors and unedited

Supplementary Information

Table of Contents

A Supplementary

A.1 Comparison of storage technologies

In Supp. Table 1, we compare *Silica* with other optical storage technologies[1–15]. The table includes the reference, media type, laser type, bits per voxel, capacity, voxel pitches (dx and dy), number of **written** layers, **demonstrated** write throughput, laser repetition rate, number of pulses per voxel, write efficiency, energy per voxel, lifetime, and whether a full decode system (i.e., data is stored and recovered) was demonstrated. The laser type is either femtosecond (fs) pulsed, picosecond (ps) pulsed or continuous wave (CW). If a listed technology is a commercial product, we state the capacity as reported by the manufacturer in their chosen form factor, and we assume the capacity is based on user bits. If a listed technology is an academic study, we calculate the capacity by finding the number of voxels in a 120 mm × 120 mm area based on the voxel pitches (dx and dy) and multiplying by the number of bytes per voxel and the number of written layers. Write efficiency is included only for the technologies that report optical energy required to write a single voxel. Magnetic and other commercial optical storage technologies report the total energy consumed per drive, which is not directly comparable to our energy per voxel. All estimated metrics are based on the reported experimental values used for the storage demonstration, not predictions or extrapolations along the z dimension. For listed technologies, we have extrapolated the xy-densities from reported results to ensure estimated capacities are comparable. We have not extrapolated in z from small numbers of written layers to larger numbers of layers because this would not be valid without experimental verification as, for many technologies, it is harder to write and read large numbers of layers. We exclude density as a metric as a lot of prior work reports only a few written layers and calculations would require extrapolation along the z dimension.

Supp. Table 1: Comparison of storage technologies. * based on user bits (Sec. 6.1). The following notes apply (see final column of the table): [a] Birefringent voxels. [b] Phase voxels. [c] Capacity per platter (and per drive) based on the commercially available drives. [d] Capacity per cartridge based on the commercially available drives. [e] Capacity per platter stated in the company's reported roadmap. [f] Capacity for femtosecond laser technology: double-sided platter configuration; 10 platters per cartridge. Throughput per single read/write head reported in the company's whitepaper. [g] The energy was based on one seeding pulse (30 nJ) and seven data pulses (13.5 nJ) to write each voxel. [h] The minimum pulse energy (150 nJ) and number of pulses (20) were used to calculate the energy per voxel. [i] The throughput was calculated using the exposure time (100 ms). [j] The number of pulses reported here is the lowest for the encoding. To write 4 bit up to 1×10^7 pulses are required. [k] We used the low retardance level energy to calculate the energy (600 nJ seed pulse, 390 nJ data pulse, two data pulses).

Reference	Media	Laser	Bits	Capacity TB/platter (TB/drive)	*dx* µm	*dy* µm	Layers	Throughput Mbit/s	Rep Rate MHz	Pulses	Write Efficiency nJ/bit	Energy nJ/voxel	Lifetime years	Full decode	Notes
This Study	Fused Silica	fs	3	4.8*	Sec. 4	Sec. 4	Sec. 4	25.6*	10	1	10.1*	Sec. 4	10000+	yes	a
This Study	Borosilicate	fs	2	2.0*	Sec. 4	Sec. 4	Sec. 4	65.9*	10	1	8.85*	Sec. 4	10000+	yes	b
[1,2]	HDD (HAMR)	n/a	1	3.6 (36)	n/a	n/a	n/a	2160*	n/a	n/a	n/a	n/a	<5	yes	c
[2,3]	Tape	n/a	1	50	n/a	n/a	n/a	3200*	n/a	n/a	n/a	n/a	<30	yes	d
[4]	Polymer	CW	1	0.50	n/a	n/a	n/a	n/a	n/a	n/a	n/a	n/a	100+	n/a	e
[5,6]	Ceramic	fs	1	0.25 (2.5)	n/a	n/a	n/a	40	n/a	n/a	n/a	n/a	1000+	n/a	f
[7]	Fused Silica	fs	4	0.25	1.20	1.20	50	1.8	10	8	31	124.5	10000+	n/a	g
[8]	Fused Silica	fs	4	0.18	2.00	2.00	100	0.064	1	20	750	3000	10000+	n/a	h
[9]	Fused Silica	fs	1	0.034	2.30	2.30	100	0.005	0.001	1	300	300	10000+	n/a	
[10]	Polymer	fs and CW	8	381	0.054	0.07	100	8×10^{-5}	42	4.2×10^{6}	17,000	2125	41	n/a	i
[11]	Polymer	ps	1	0.563	0.80	0.80	200	10	10	1	50	50	n/a	n/a	
[12]	Polymer	fs	6	0.018	1.33	1.33	3	n/a	82	1	0.05	0.28	n/a	n/a	
[13]	Glass Hybrid	fs	2	0.026	0.65	0.65	3	8×10^{-5}	80	n/a	2813	5625	600+	n/a	
[14]	Glass Hybrid	fs	4	0.002	3.00	3.00	3	0.4	10	100	1725	6900	4+	n/a	j
[15]	Fused Silica	fs	4	0.003	1.50	1.50	1	n/a	0.1	3	345	1380	10000+	n/a	k

A.2 Decoding without a CNN

We can decode without a CNN for quick lab experiments where speed is prioritized over accuracy. For birefringent voxels we compute the pixelwise azimuth angle from the raw images and then apply adaptive equalization[16] and thresholds to the angle to obtain a symbol value for each voxel. For phase voxels we apply thresholds on the intensity image.

A.3 Scanning geometry

The seed and data pulses are focused and scanned inside the media. The media is moved at a velocity V_s in the x direction as the polygon scans the beam at a speed V_f in the y direction. Columns of voxels are formed with a pitch $\Delta_x = V_s T_s$ where T_s is the time per polygon facet. Columns are tilted at an angle $\theta_s \approx V_s/V_f$. Angle θ_s is typically smaller than a few milliradians.

The velocity of the foci inside the media is given by

$$V_f = 2\frac{f_{obj}\omega_{pol}}{M_{relay}}$$

where f_{obj} is the focal length of the objective lens, M_{relay} is the optical magnification between polygon and objective, and ω_{pol} is the angular velocity of the polygon. $T_s = 2\pi/(N_{facet}\omega_{pol})$ where N_{facet} is the number of facets of the polygon.

A.4 Polarization grating beam splitter

Here we describe how tuneable beam splitting can be realized using a pair of polarization gratings (*PGs*). A *PG* is a geometric phase (or Pancharatnam-Berry phase) optical element[17] in which birefringence is patterned periodically in space. For our purposes, a *PG* is a simple diffraction grating with period Λ and unit grating vector $\hat{\mathbf{g}}$ perpendicular to the grating lines. When the input light is elliptically polarized, the *PG* splits the input beam (wavelength λ) into left-handed circular and right-handed circular polarizations. In the small angle approximation, the LHCP component of the input beam is deflected by an angle $\phi \approx \frac{\lambda}{\Lambda}$ and the RHCP component is deflected by $-\phi$ relative to the input beam direction. The *PG* causes the wave vector of input LHCP light to change by $\Delta\mathbf{k} = \frac{2\pi}{\Lambda}\hat{\mathbf{g}}$. Two *PGs* can achieve a tuneable splitting angle as follows. Let the changes in the wave vectors to LHCP by two *PGs* be $\Delta\mathbf{k}_1$ and $\Delta\mathbf{k}_2$. The total change in the wave vector is given by $\delta\mathbf{k} = \Delta\mathbf{k}_1 - \Delta\mathbf{k}_2$ (sign reversed for RHCP). The minus sign appears because the handedness of the circular polarization is flipped after transmission through each *PG*. In terms of the grating vectors, $\delta\mathbf{k} = \frac{2\pi}{\Lambda}(\hat{\mathbf{g}}_1 - \hat{\mathbf{g}}_2)$, where we have assumed that both gratings have the same period but different orientations. We now write $\hat{\mathbf{g}}_j = (\cos\theta_j, \sin\theta_j)$ where θ_j is the angle of the *j*-th *PG* about the optical axis. Then,

$$\delta\mathbf{k} = \frac{4\pi}{\Lambda}\sin\left(\frac{\theta_1 - \theta_2}{2}\right)\left(\sin\frac{\theta_1 + \theta_2}{2}, \cos\frac{\theta_1 + \theta_2}{2}\right) \quad (1)$$

This equation shows that the change in the direction of propagation after transmission through both *PGs* can be controlled by changing the relative angles of the two *PGs*, and that the angle of the split plane can be controlled by rotating both *PGs* together. We can tune the amplitude ratio between the two output circularly-polarized beams by changing the ellipticity (χ) of the input light: $A_{\mathrm{LH}}/A_{\mathrm{RH}} = (1-\chi)/(1+\chi)$.

We realize our tuneable *PG*-based splitter using input linear polarization, a quarter-wave plate (QWP) to tune the ellipticity, and two *PGs* mounted on motorized rotary stages to control the split angle and plane (Supp. Fig. 1). For pseudo-single pulse writing, the split angle is set so that the distance between the seed and data pulses is a multiple of voxel pitch in the media and the split plane is set to be parallel to the beam scanning direction.

A.5 Multibeam thermal simulation method

We simulated the temperature distribution during voxel writing by solving the thermal diffusion equation with multiple heat sources. For simplicity, we assumed that the temperature dependence of the heat capacity and density of glass are negligible, which enables us to solve the thermal diffusion equation as a linear differential equation[18]:

$$\frac{\partial}{\partial t}T(t,\mathbf{r}) = D_{\mathrm{th}}\nabla^2 T(t,\mathbf{r}) + \frac{1}{\rho C_p}\frac{\partial}{\partial t}Q(t,\mathbf{r}) \tag{2}$$

where $T(t, \mathbf{r})$ is the temperature distribution at time t and at the position $\mathbf{r}$, D_{th}, ρ and C_p are the thermal diffusivity, density, and heat capacity of glass, respectively, and $Q(t, \mathbf{r})$ is the sum of all the heat sources of photoexcitations which happened in different locations and at different times. If each heat source is represented by $q(t, \mathbf{r}; t_j, \mathbf{R}_{i,j})$, $Q(t, \mathbf{r})$ is expressed by

$$Q(t, \mathbf{r}) = \sum_{j} \sum_{k} q(t, \mathbf{r}; t_j, \mathbf{R}_{j,k}) \tag{3}$$

where j is the index of time at which photoexcitation happens, k is the index of the beams and $\mathbf{R}_{j,k}$ is the location at which a laser pulse of beam k is focused at the time t_j. The temperature distribution can be given by the summation of the temperature changes by all the heat sources because the heat equation is linear,

$$T(t, \mathbf{r}) = T_0 + \sum_{j} \sum_{k} \Delta T_{j,k}(t, \mathbf{r}) \tag{4}$$

where T_0 is the ambient temperature and $\Delta T_{j,k}(t, \mathbf{r})$ is the temperature change by each heat source, $q(t_j, \mathbf{R}_{j,k})$, which is generated by the photoexcitation at the time t_j and at the position $\mathbf{R}_{j,k}$. $\Delta T_{j,k}(t, \mathbf{r})$ is given by individual thermal diffusion equation:

$$\frac{\partial}{\partial t}\Delta T_{j,k}(t, \mathbf{r}) = D_{\mathrm{th}} \nabla^2 \Delta T_{j,k}(t, \mathbf{r}) + \frac{1}{\rho C_p}\frac{\partial}{\partial t} q(t, \mathbf{r}; t_j, \mathbf{R}_{j,k}) \tag{5}$$

For simplicity, we assume that each heat source is given by a Gaussian function,

$$q(t, \mathbf{r}; t_j, \mathbf{R}_{j,k}) = q(t - t_j, \mathbf{r} - \mathbf{R}_{j,k}) \tag{6}$$

$$q(t, \mathbf{r}) = \Delta T_{ex} \rho C_p H(t) \exp\left(-\frac{x^2 + y^2}{w_{th0}^2} - \frac{z^2}{l_{z0}^2} \right) \quad (7)$$

where ΔT_{ex} is the highest temperature rise by a single photoexcitation, $H(t)$ is the Heaviside step function, w_{th0} and l_{z0} are the width and length of each heat source determined by the photoexcited region. The solution of the temperature change by $q(t, \mathbf{r})$ is given by

$$\Delta T_q(t, \mathbf{r}) = \Delta T_{ex} H(t) \left(\frac{w_{th0}}{w_{th}(t)} \right)^2 \left(\frac{l_{z0}}{l_z(t)} \right) \exp\left(-\frac{x^2 + y^2}{w_{th}(t)^2} - \frac{z^2}{l_z(t)^2} \right) \quad (8)$$

$$w_{th}(t) = \sqrt{w_{th0}^2 + 4D_{th}(t)} \quad (9)$$

$$l_z(t) = \sqrt{l_{z0}^2 + 4D_{th}(t)} \quad (10)$$

As a result,

$$T(t, \mathbf{r}) = T_0 + \sum_j \sum_k \Delta T_q(t - t_j, \mathbf{r} - \mathbf{R}_{j,k}) \quad (11)$$

All simulations used w_{th0}=0.1 µm, l_{z0}=2.0 µm, and D_{th}=0.66 µm^2/µs (thermal diffusivity of BOROFLOAT® 33).

References

1. Mellor, C. *Seagate still HAMRing away at the 100 TB disk drive decades later* https://www.theregister.com/2025/06/09/hamr_100_tb_drive_feature/ (2025).
2. Lunt, B. M., Kemp, D., Linford, M. R. & Chiang, W. How Long Is Long-Term? - An Update. *Archiving Conference* **21,** 56–56. doi:10.2352/issn.2168-3204.2024.21.1.11 (2024).
3. *IBM TS1170 Tape Drive* https://www.ibm.com/downloads/documents/us-en/107a02e95cc8f7f4 (2025).
4. Singer, K. D. High-capacity optical data storage for active archives. **PC13389** (eds Miyata, S., Yatagai, T. & Koike, Y.) PC1338903. doi:10.1117/12.3045635 (2025).
5. *Cerabyte White Paper* https://www.cerabyte.com/wp-content/uploads/2025/02/Cerabyte-White-Paper-2-25.pdf (2025).
6. Pflaum, C. *Ceramic Nano Memory: Data Storage for the Yottabyte Era* https://storagedeveloper.org/sites/default/files/SDC/2023/presentations/SNIA-SDC23-Pflaum-Ceramic-Nano-Memory_2.pdf (2023).
7. Lei, Y. *et al.* High speed ultrafast laser anisotropic nanostructuring by energy deposition control via near-field enhancement. *Optica* **8,** 1365–1371. doi:10.1364/OPTICA.433765 (2021).

8. Wang, H. *et al.* 100-Layer Error-Free 5D Optical Data Storage by Ultrafast Laser Nanostructuring in Glass. *Laser & Photonics Reviews* **16,** 2100563. doi:10.1002/lpor.202100563 (2022).

9. Imai, R. *et al.* 100-Layer recording in fused silica for semi permanent data storage. *Japanese Journal of Applied Physics* **54,** 09MC02. doi:10.7567/JJAP.54.09MC02 (2015).

10. Zhao, M. *et al.* A 3D nanoscale optical disk memory with petabit capacity. *Nature* **626,** 772–778. doi:10.1038/s41586-023-06980-y (2024).

11. Walker, E., Dvornikov, A., Coblentz, K., Esener, S. & Rentzepis, P. Toward terabyte two-photon 3D disk. *Opt. Express* **15,** 12264–12276. doi:10.1364/OE.15.012264 (2007).

12. Zijlstra, P., Chon, J. W. M. & Gu, M. Five-dimensional optical recording mediated by surface plasmons in gold nanorods. *Nature* **459,** 410–413. doi:10.1038/nature08053 (2009).

13. Zhang, Q., Xia, Z. & Gu, M. High-capacity optical long data memory based on enhanced Young's modulus in nanoplasmonic hybrid glass composites. *Nature Communications* **9,** 1183. doi:10.1038/s41467-018-03589-y (2024).

14. Royon, A. *et al.* Silver Clusters Embedded in Glass as a Perennial High Capacity Optical Recording Medium. *Advanced Materials* **22,** 5282–5286. doi:10.1002/adma.201002413 (2010).

15. Gao, J., Yan, Z., Wang, H. & Zhang, J. Rapid generation of birefringent nanostructures by spatially and energy manipulated femtosecond lasers for ultra-high

speed 5D optical recording exceeding MB/s. *Opt. Express* **32,** 32879–32894. doi:10.1364/OE.530732 (2024).

16. Godard, D. Self-Recovering Equalization and Carrier Tracking in Two-Dimensional Data Communication Systems. *IEEE Transactions on Communications* **28,** 1867–1875. doi:10.1109/tcom.1980.1094608 (1980).

17. Bomzon, Z., Kleiner, V. & Hasman, E. Pancharatnam–Berry phase in space-variant polarization-state manipulations with subwavelength gratings. *Opt. Lett.* **26,** 1424–1426. doi:10.1364/OL.26.001424 (2001).

18. Shimizu, M. *et al.* Mechanism of heat-modification inside a glass after irradiation with high-repetition rate femtosecond laser pulses. *Journal of Applied Physics* **108,** 231112. doi:10.1063/1.3046101 (2010).

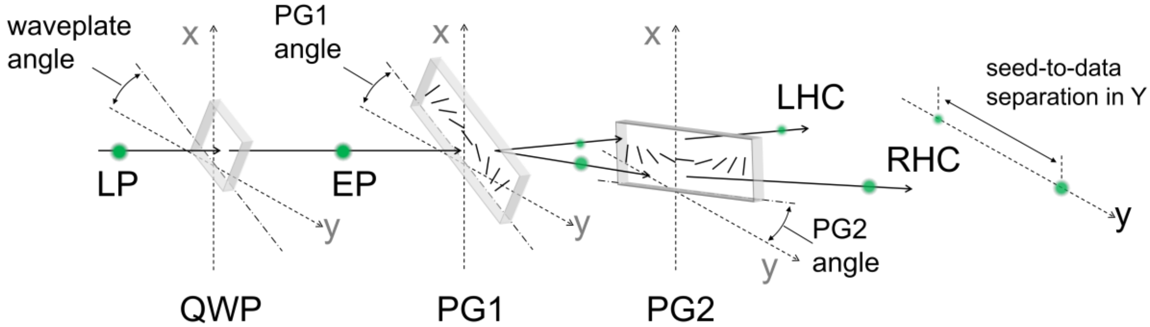

Supp. Figure 1: *PG* beam splitter. The light propagates from the left to right. The input light is linearly polarized (LP). The QWP converts the input light to elliptically polarized (EP) light. The first *PG* (PG1) splits the EP light into left-handed circular (LHC) and right-handed circular (RHC) polarizations. The second *PG* (PG2) deflects each polarization in opposite directions. The optics can be rotated independently around the optical axis by a motorized rotary stage.